Impact of Air–Sea Coupling on the Madden–Julian Oscillation in a General Circulation Model

HARRY H. HENDON

NOAA CIRES Climate Diagnostics Center, Boulder, Colorado

(Manuscript received 7 September 1999, in final form 3 March 2000)

ABSTRACT

The impact of air–sea coupling on the dynamics of the tropical Madden–Julian oscillation (MJO) is investigated with an atmospheric general circulation model (GCM) coupled to an ocean mixed layer model. In the uncoupled GCM, where climatological sea surface temperature (SST) is specified, realistic space–time spectra of near-equatorial zonal wind and precipitation are produced, with power concentrated at eastward wavenumbers 1–3 with periods of 35–90 days. However, the simulated MJO is roughly 50% stronger than observed, largely resulting from enormous activity during northern summer. Furthermore, during southern summer, when the observed MJO is most dominant across the Indian and western Pacific Oceans, intraseasonal variance in the uncoupled model is overly concentrated to the north and east of Australia with little activity extending into the equatorial Indian Ocean. Contrary to other recent modeling studies, coupling did not alleviate either of these problems nor did it have any other appreciable impact on the model's MJO.

Feedback of the SST anomalies onto the MJO, both observed and diagnosed in other coupled models, appears to result from correlation of positive equatorial SST anomalies across the warm pool with surface low pressure to the east of the convective anomaly. This feedback is insignificant in the present coupled model because the SST anomalies, besides being too weak and not spatially coherent, do not systematically exhibit the requisite phasing with the surface pressure. The observed SST anomalies result from a combination of shortwave radiation and latent heat flux, whereby reduced shortwave radiation associated with enhanced convection slightly leads enhanced latent heat flux associated with increased surface westerlies. The model does produce realistic shortwave radiation anomalies, but its latent heat flux anomalies are too weak and do not constructively add with the shortwave radiation anomalies. It is concluded that coupling is not a panacea for problems of simulating the MJO in uncoupled GCMs and that coupling, if it is important, depends critically on the structure of the surface fluxes produced by the MJO.

1. Introduction

There is growing interest in the role that air–sea interaction may play for the dynamics of the Madden–Julian oscillation (MJO; Flatau et al. 1997; Sperber et al. 1997; Wang and Xie 1998; Waliser et al. 1999). Such interest has been motivated by the generally poor performance of general circulation models (GCMs) in simulating and forecasting the MJO (e.g., Slingo et al. 1996; Hendon et al. 2000). Models with prescribed sea surface temperatures (SST) typically produce MJOs that move eastward too fast, are too weak, and have incorrect seasonality. The speculation is that interactive SST may be an important neglected physics.

The case that air–sea interaction is important for the dynamics of the MJO stems from observations that SST fluctuates on intraseasonal timescales across the warm pool of the equatorial Indian and western Pacific Oceans (e.g., Krishnamurti et al. 1988) and that these fluctuations are coherent with the MJO (e.g., Zhang 1996). Observations taken during the Coupled Ocean–Atmosphere Response Experiment revealed local swings of SST in excess of 1°C in association with passage of the MJO (Gutzler et al. 1994; Weller and Anderson 1996). These fluctuations in SST are understood to result primarily from variations of latent heat flux and surface shortwave radiation, which act in unison to perturb the surface heat flux because enhanced latent heat flux during the westerly phase of the MJO slightly lags (~5 days) decreased surface shortwave radiation during its cloudy phase (Hendon and Glick 1997; Lau and Sui 1997; Shinoda et al. 1998). One-dimensional mixed layer processes primarily govern these large-scale, intraseasonal SST variations in the warm pool (Shinoda and Hendon 1998) because the mean winds are weak, the mean thermocline is deep, and horizontal SST gradients are weak. However, horizontal advection may be important near the equator for some stronger events (e.g., Feng et al. 1998).

Corresponding author address: Harry Hendon, Climate Diagnostics Center, Mail Code R/E/CD, 325 Broadway, Boulder, CO 80303-3328.
E-mail: hhh@cdc.noaa.gov

The potential feedback of these intraseasonal SST variations to the dynamics of the MJO has been addressed in three recent modeling studies. Using a single baroclinic mode atmospheric model coupled to a simplified upper-ocean model, Wang and Xie (1998) found significant feedback from the ocean mixed layer to the moist wave dynamics at intraseasonal timescales. As a result of coupling, the simulated MJO was destabilized and its eastward propagation was reduced to realistic speeds. This destabilization resulted from generation of equatorial SST anomalies that realistically lead the MJO-induced convective anomalies by just less than a quarter-cycle and are in phase with surface low pressure. The warm SST anomalies act to further reduce the surface pressure, which increases zonal convergence in the winds and increases convergence into the convective anomaly. Without coupling to the ocean mixed layer, no unstable modes in the atmosphere were found. In this model not only did air–sea coupling produce a more realistic MJO, it also provided the mechanism for growth.

Flatau et al. (1997) investigated the impact of interactive SSTs on the simulated MJO in a GCM. Ocean mixed layer variations were simply represented by an empirical relationship between surface wind speed and SST, whereby enhanced surface westerlies cause surface cooling and enhanced easterlies cause surface warming. Contrary to Wang and Xie (1998), the uncoupled model did produce an MJO, but with many of the shortcomings reported by Slingo et al. (1996). Inclusion of interactive SSTs increased the amplitude and slowed the eastward phase speed of the model's MJO. Flatau et al. speculate that increased strength of the MJO results from the occurrence of warm SSTs to the east of the convective anomaly, which directly destabilize the atmosphere by increasing the moist static energy via the nonlinear increase of saturation vapor pressure with temperature. However, Waliser et al. (1999) argue that the sensitivity of the saturation vapor pressure to the intraseasonal variation in SST is too weak to explain the increase in moist static energy.

Most recently, Waliser et al. (1999) coupled an atmospheric GCM to an anomaly mixed layer model, which treats the ocean mixed layer as a fixed slab and predicts SST anomalies in response to anomalous surface heat flux. Again, the uncoupled GCM did produce an MJO, but it was too weak, moved eastward too fast, and exhibited poor seasonality (relatively too strong during northern summer). Coupling alleviated these problems. Waliser et al. argue, similar to Wang and Xie (1998), that the generated SST anomalies to the east of the convection act to further reduce the surface pressure there. But they argue it is the meridional convergence that increases and promotes enhanced convection via frictional wave conditional instability of the second kind (CISK).

The present study extends these previous studies by exploring the impact of coupling on the MJO in an atmospheric GCM coupled to a comprehensive ocean mixed layer model. Shinoda and Hendon (1998) showed that observed SST variability driven by the MJO is well simulated by such a one-dimensional mixed layer model when forced by observed surface fluxes. The present mixed layer model, similar in its sophistication to that used by Shinoda and Hendon (1998), responds not only to surface heat flux variations but to freshwater fluxes and momentum fluxes. These fluxes are important to the intraseasonal evolution of the mixed layer temperature in the warm pool (Anderson et al. 1996; Shinoda and Hendon 1998). Furthermore, the model accounts for a variable mixed layer depth and penetration of shortwave radiation through the base of the mixed layer, which has important consequences during the calm/clear phase of the MJO when the mixed layer shoals to $\sim$10-m depth (Shinoda and Hendon 1998).

The strategy for this study is to contrast the MJO activity in the coupled model with that in the uncoupled model where the climatological SSTs from the coupled run are prescribed. The impact of coupling on the model's MJO turns out to be minimal. While this may at first appear to be a null (and uninteresting) result, subsequent comparison with observations and analysis to uncover why coupling has no impact sheds light onto both the dynamics of the MJO and the subtleties of air–sea coupling in the warm pool.

2. Model details and observational data

The atmospheric model is a version of the Geophysical Fluid Dynamics Laboratory (GFDL) global spectral GCM with rhomboidal truncation at wavenumber 30 (see Gordon and Stern 1982 for a detailed description of an earlier version of the model). It has 14 sigma levels in the vertical with the lowest level at $\sigma = 0.997$. The model uses moist convective adjustment with a 100% relative humidity threshold. Stratiform clouds form and large-scale precipitation occurs when the relative humidity exceeds 100%.

The atmospheric model is coupled to a one-dimensional ocean mixed layer model at each grid point. Details of the mixed layer model and the coupling procedure are provided by Alexander et al. (2000, hereafter ASD). In summary, the mixed layer model is based on Gaspar (1988) and consists of a bulk mixed layer of variable depth atop a layered model extending to a depth of 1000 m. Temperature of the mixed layer changes due to surface heat flux variations, entrainment, and vertical diffusion. The mixed layer deepens due to convective adjustment and entrainment. When shoaling, the mixed layer depth is computed diagnostically by assuming a balance among wind mixing, buoyancy forcing, and dissipation. Salinity of the mixed layer is also predicted, with the freshwater flux specified as the difference between precipitation and evaporation. Temperature and salinity below the mixed layer change by convective adjustment, vertical diffusion, and damping. Penetrative

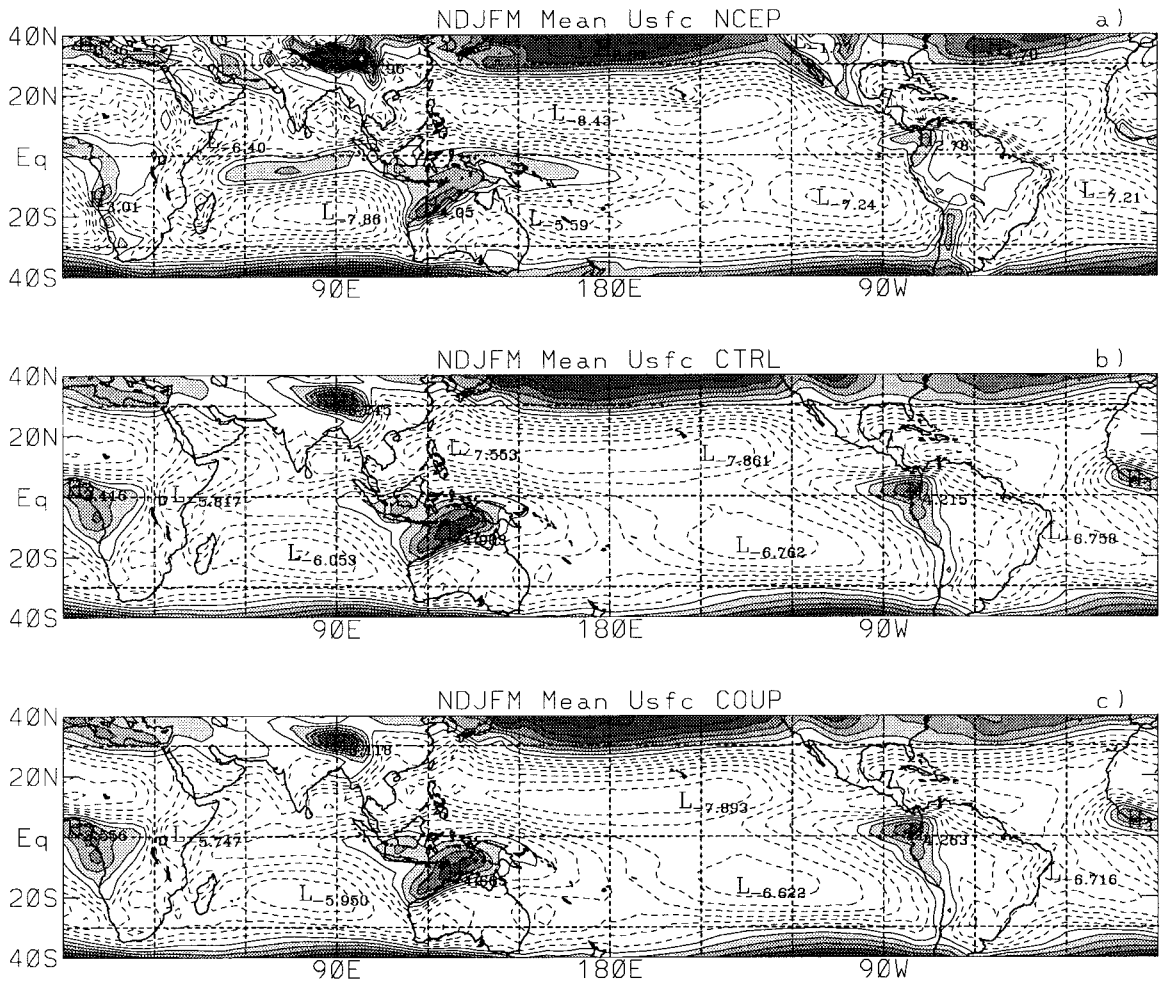

FIG. 1. Nov–Mar mean surface zonal wind from (a) the NCEP–NCAR reanalysis 1979–98, (b) the control run, and (c) the coupled run. The contour interval is 1 m s^{-1} with negative contours dashed. Westerly winds greater than 1 m s^{-1} are shaded.

shortwave radiation also affects the temperature to a depth of 300 m. Temperature and salinity at all model levels are damped to their monthly mean climatological values with a 10-yr timescale, which accounts for neglected processes such as heat transport as a function of depth.

Heat (shortwave and longwave radiation, and latent and sensible heat), momentum, and freshwater are exchanged once per day across the model's air–sea interface. The sensible and latent heat fluxes and surface stress are computed with standard bulk aerodynamic formulas where the exchange coefficients have a constant value of 1×10^{-3}. The wind speed, air temperature, and humidity in these formulas are taken from the lowest model level. The SST is taken as the temperature of the mixed layer.

Heat and salt flux correction are applied at each grid point in order for the simulated climate to be realistic. These flux corrections account for neglected processes in the ocean (primarily horizontal advection) and errors in the mean surface fluxes. The flux corrections are derived from a 20-yr integration of the mixed layer model forced with surface fluxes from a separate integration of the atmospheric GCM where the observed monthly mean SSTs were used as the lower boundary condition. After each time step of the mixed layer model, the mixed layer salinity and temperature were set to their climatological values and the differences were saved. This process was repeated for 20 yr from which monthly mean flux corrections were calculated. Details of the seasonal variation of the heat and salinity flux corrections are provided by ASD.

The coupled model was run for 50 yr. Here the first 20 yr of the integration are examined. A 20-yr control integration also was performed with the atmospheric GCM, where the monthly mean climatology of SST produced by the coupled run was prescribed as the lower boundary condition. Using the climatological SST produced from the coupled run ensures that both the coupled and uncoupled models feel the same mean lower

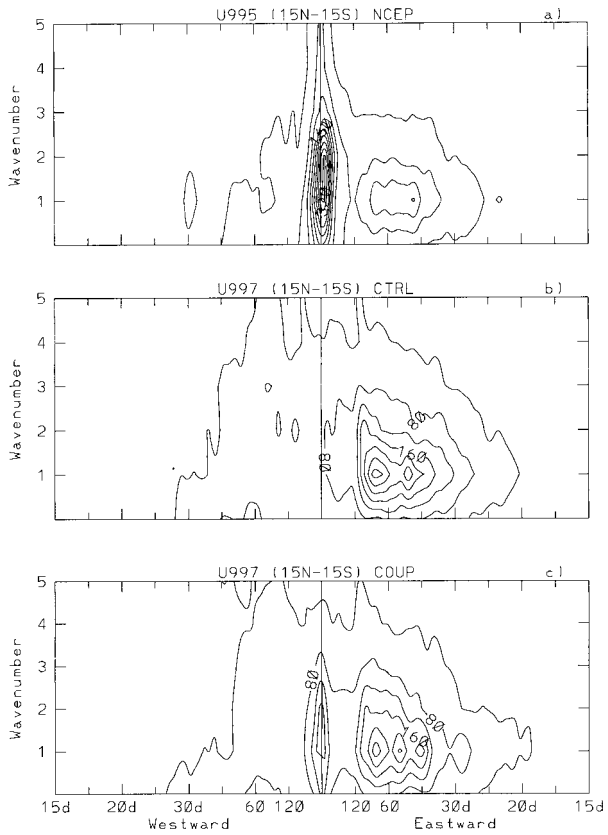

FIG. 2. Wavenumber frequency spectra for the surface zonal wind from (a) the NCEP–NCAR reanalysis 1979–98, (b) the control run, and (c) the coupled run. Power was computed at each latitude between 15°N and 15°S and then averaged. The climatological seasonal cycle was removed prior to computation of the spectra. The frequency bandwidth is 1/7300 cycles day^{-1} and the contour interval is 4×10^{-4} m^2 s^{-2}.

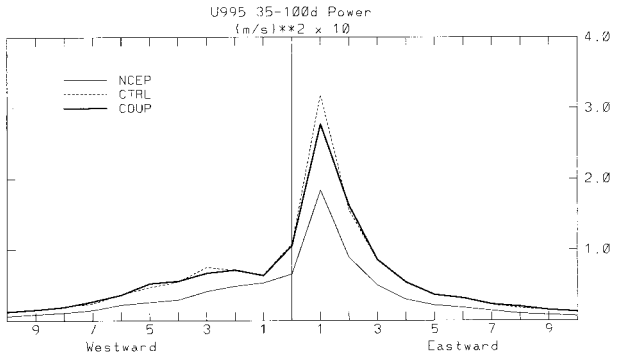

FIG. 3. Wavenumber spectra for the surface zonal wind from the NCEP–NCAR reanalysis (thin curve), the control run (dashed curve), and the coupled run (heavy curve). Power was integrated for periods of 35–90 days and averaged for each latitude between 15°N and 15°S.

boundary condition. Nonetheless, the climatological SST produced by the coupled model is very realistic (differences are ~0.25°C across the warm pool) due to the flux correction and weak damping to climatology.

For this study of the impact of air–sea coupling on the MJO, daily mean surface data are analyzed. These include winds, temperature, and humidity at the lowest model level ($\sigma = 0.997$); sea level pressure; and the temperature of the ocean mixed layer (taken to be the model's SST). Daily mean surface fluxes of heat (latent, sensible, and shortwave and longwave radiation) and precipitation are also utilized.

MJO activity in the models is also compared to observed activity as depicted in 20 yr (1979–98) of National Centers for Environmental Prediction–National Center for Atmospheric Research (NCEP–NCAR) reanalyses (Kalnay et al. 1996). Winds, temperature, and humidity at the lowest analysis level ($\sigma = 0.995$), sea level pressure, surface skin temperature, and surface heat fluxes are utilized. Shinoda et al. (1999) show that the intraseasonal variation of sensible and latent heat flux and net longwave radiation are reasonably depicted in the reanalysis but that there are significant deficiencies in the net surface shortwave radiation. Hence, net surface shortwave radiation was estimated from top of the atmosphere outgoing longwave radiation (OLR) as described by Shinoda et al. (1998). OLR is also used as a proxy for tropical deep convection. Details of the daily OLR data are provided by Liebmann and Smith (1996). Prior to comparison with the model data, all of the observed datasets were transformed onto the model's R30 Gaussian grid (96×80).

3. Mean fields and characteristics of intraseasonal variability

a. Mean fields

The mean climates from the coupled and control runs are similar to the climate from the GFDL GCM forced with observed SSTs (Alexander and Scott 2000), because the climatological SSTs from the coupled run are similar to observed. Here, some of the properties of the climate from the coupled and control runs that are relevant to the MJO are discussed.

The mean surface zonal wind for November–March is displayed in Fig. 1. This extended southern summer season is shown because the observed MJO is strongest then. Also shown in Fig. 1 is the mean zonal wind from the NCEP–NCAR reanalysis. Immediately apparent is that the climate of the two model runs are nearly identical. Both the control and coupled runs produce stronger than observed monsoonal westerlies over Africa, northern Australia, and northern South America, and weaker than observed monsoonal westerlies (the models actually produce easterlies) over the equatorial Indian and western Pacific Oceans. The limited longitudinal extent of the monsoonal westerlies in the Indian and western Pacific Oceans is reflected in the mean precipitation (not shown), which also is concentrated to the north of Australia and does not extend into the Indian and western Pacific Oceans.

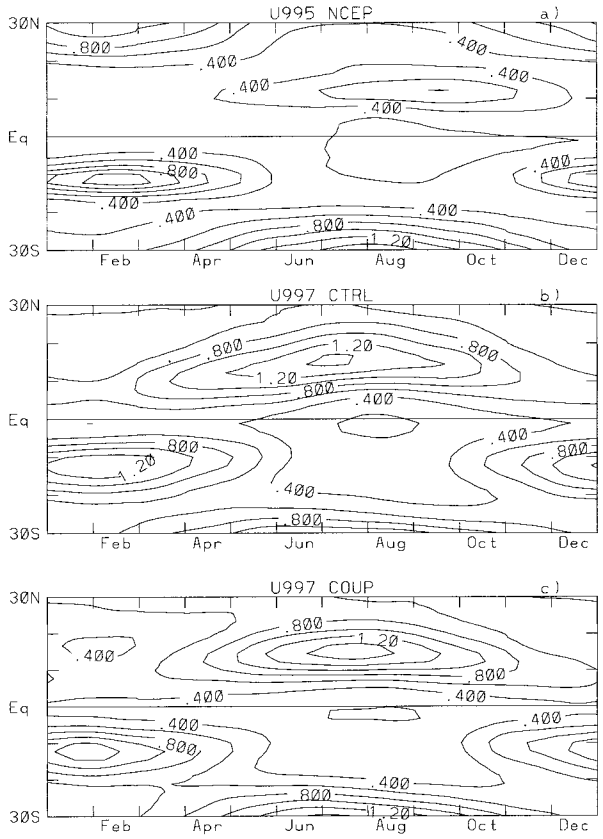

FIG. 4. Seasonal cycle of power of the surface zonal wind for eastward wavenumbers 1–3 with periods of 35–90 days. Contour interval is 2×10^{-1} m^2 s^{-2}.

The lack of mean surface westerlies across the bulk of the warm pool has a direct impact on the sign of the latent heat flux anomalies driven by the MJO. The observed latent heat flux anomalies result primarily from wind speed anomalies associated with enhanced surface westerlies just to the west of enhanced convection (e.g., Hendon and Glick 1997). These same enhanced westerlies would produce negative latent heat flux anomalies across most of the warm pool in the GFDL model. Thus, the distribution of net surface heat flux anomalies and the subsequent air–sea interaction across the warm pool in the model will be adversely affected (discussed in detail below).

The mean surface specific humidity also affects the latent heat flux. The surface specific humidity is significantly higher across the warm pool in the model than is observed (20–21 $\times$ 10^{-3} kg kg^{-1} compared to 18–19 $\times$ 10^{-3} kg kg^{-1}). Furthermore, the warm pool SST in the model is systematically $\sim$0.25°C colder than observed. Thus, the mean difference between the saturated specific humidity at the SST and the actual specific humidity at the surface is about 20% lower in the model than is observed. Assuming that the latent heat flux anomalies across the warm pool are driven primarily by wind speed variations, the same wind speed anomaly in the model will produce about a 20% weaker latent heat flux anomaly than observed.

Finally, the mean mixed layer depth in the warm pool will determine the sensitivity of the SST variability to the imposed surface flux anomalies. ASD show that the model's mean mixed layer depth across the warm pool is between 10 and 40 m, which compares favorably with observations. Hence, SST in the coupled model is expected to exhibit realistic sensitivity to the surface flux anomalies produced by the model's MJO.

b. Intraseasonal variability

Space–time spectra of the surface zonal wind, using the entire 20-yr records, are shown in Fig. 2. Power was computed at each latitude between 15°N and 15°S and then averaged. There are three important aspects about these spectra that are immediately apparent. The first is that coupling has little impact on intraseasonal variability of near-equatorial surface zonal wind. That is, the spectra for the coupled and control runs are nearly identical for periods less than 100 days. This is also true of other related fields such as precipitation and upper-tropospheric zonal wind. The second is that this model produces a very realistic distribution of power in the intraseasonal band traditionally attributed to the MJO. That is, power is concentrated at eastward wavenumber 1 with periods of 35–90 days, which compares favorably to the observed spectrum. The typical problem of GCMs producing an MJO that has too-high frequency (e.g., Slingo et al. 1996) is not manifested in this GFDL GCM, coupled or uncoupled (see also Hayashi and Golder 1993). Third, the models produce an MJO with about twice as much power (or about 40% greater amplitude) as is observed. Also apparent is the lack of interannual variability at low wavenumbers in the control run, presumably because it was forced with climatological SSTs. The coupled run does exhibit enhanced power at interannual periods, but it is much weaker than observed. This result is expected because much of the observed interannual variability in near equatorial surface zonal wind results from the El Niño–Southern Oscillation, whose dynamics are absent in the present coupled model. Further discussion of interannual variability in the coupled run is provided by ASD.

Closer inspection of the model spectra suggests that coupling has acted to slightly weaken the MJO. This is emphasized in Fig. 3, which shows power integrated between 35- and 90-day periods as a function of zonal wavenumber. The spectral peak at zonal wavenumber 1 is slightly weaker in the control run. While this slight difference may be significant, the focus of this study is to understand why coupling did not have a more appreciable impact on the MJO.

One benefit of coupling for the MJO reported by Waliser et al. (1999) is that the seasonality was improved. Observed MJO activity is strongest in November–April (Salby and Hendon 1994). Waliser et al. reported cou-

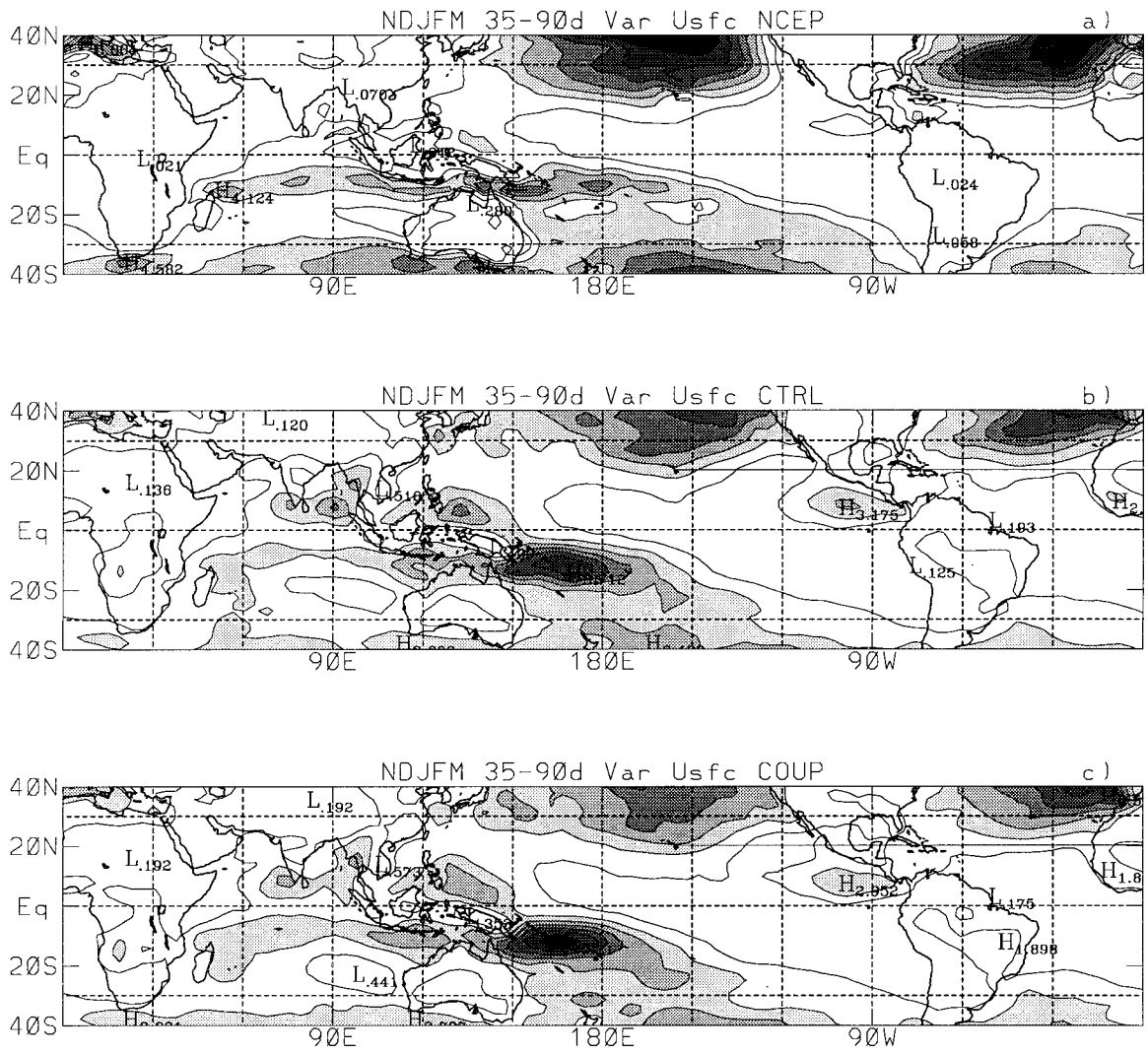

FIG. 5. Intraseasonal (35–90 days) variance for Nov–Mar of surface zonal wind from (a) NCEP–NCAR, (b) the control run, and (c) the coupled run. Contour intervals are 1 $m^2\ s^{-2}$, with values greater than 2 $m^2\ s^{-2}$ shaded.

pling produced a marked increase of MJO events during December–March and no change for June–August. Here, the seasonality of the MJO is determined following Salby and Hendon (1994), whereby power of the surface zonal wind is integrated for eastward zonal wavenumbers 1–3 with periods of 35–90 days and plotted as a function of time of year (Fig. 4). Similar results are obtained using upper-tropospheric zonal wind and OLR or precipitation. The observed distribution shows a twofold increase in power during southern summer over northern summer. On the other hand, both the coupled and control runs exhibit greater power during northern summer than during southern summer. Hence, coupling has little impact in alleviating the poor seasonality in the uncoupled model. Interestingly, during southern summer, when the observed MJO is most dominant, the coupled and control runs produces eastward power with realistic amplitude and location (near 10°S). The fact that the coupled and uncoupled models produce an MJO with double the observed power, when the entire year is considered (Fig. 2), evidently results from the enormous and unrealistic activity in the Northern Hemisphere during boreal summer.

The focus of the remainder of the paper is on the impact of coupling on the MJO during southern summer, because this is when the observed MJO is most dominant and exhibits the strongest interaction with the warm pool (e.g., Hendon and Glick 1997). The nature of the enormous intraseasonal variability during northern summer in these model runs is the subject of a future study.

The distribution of intraseasonally filtered (periods of 35–90 days) surface zonal wind variance for November–March is shown in Fig. 5. Intraseasonal filtering was accomplished by first tapering the 180-day segment beginning on 15 October each year with a cosine tapered rectangular window applied to the first and last 5% of

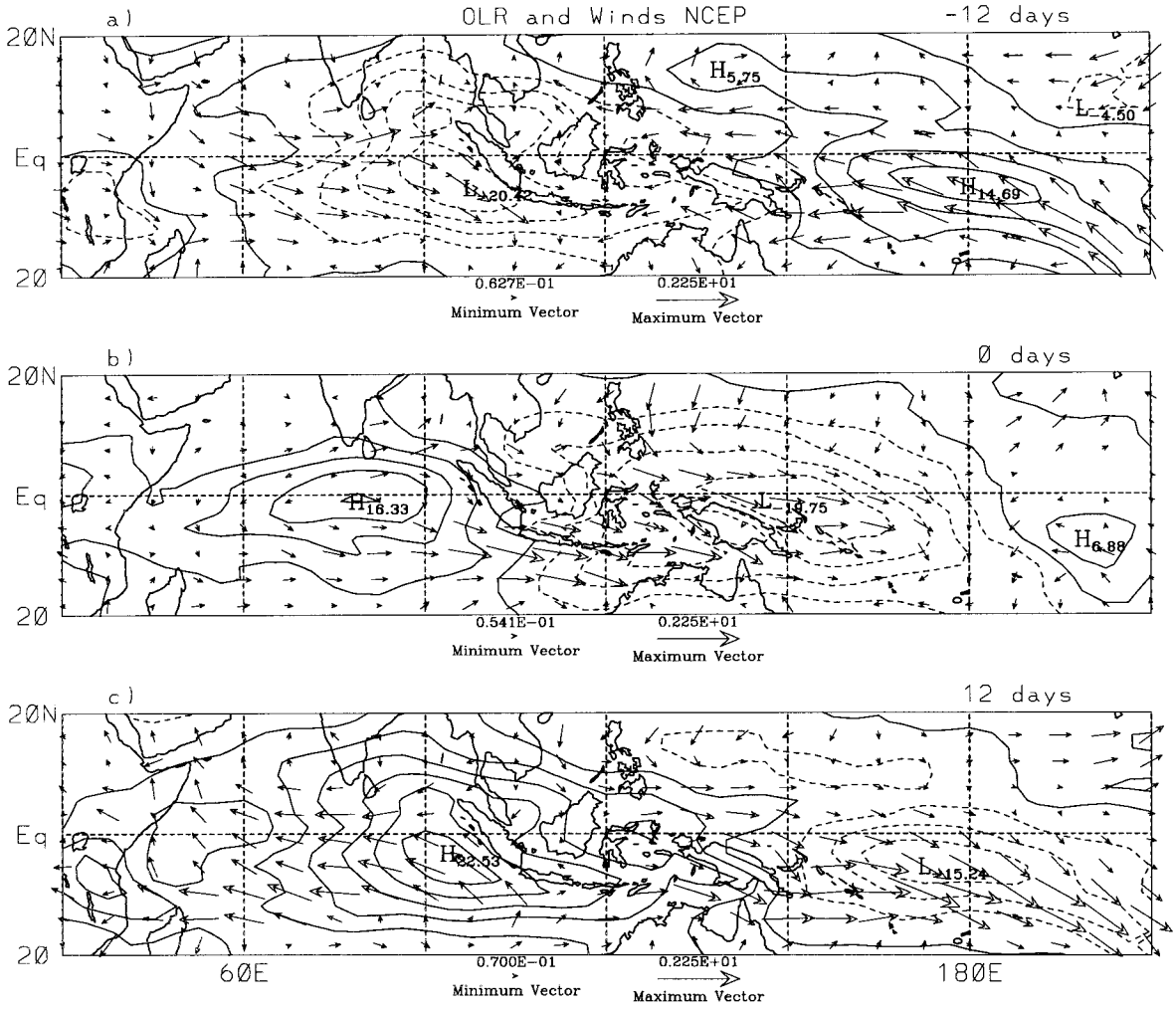

FIG. 6. Regression of observed OLR and surface winds onto OLR at the base point (0°, 150°E) for (a) lag −12 days, (b) lag 0 days, and (c) lag +12 days. OLR at the base point was filtered to eastward wavenumbers 1–3 for periods of 35–90 days and its sign was reversed to be consistent with rainfall. Anomalies are shown for a 1.5 standard deviation anomaly of the base point (=15 W m^{-2}). Contour interval for OLR is 4 W m^{-2}. The maximum amplitude of the wind vectors is 2.25 m s^{-1}.

the time series. Each segment was then Fourier transformed, retaining periods of 35–90 days. Again, little difference between the coupled and control runs is seen. They both exhibit an unrealistic concentration of variance concentrated to the east of Australia. This discrepancy is even more pronounced for the intraseasonal precipitation variance (not shown), which is consistent with the model's concentration of monsoonal westerlies (Fig. 1) and mean precipitation to the north and east of Australia and a lack of westerlies and precipitation across the equatorial Indian Ocean. Hence, while the model's space–time spectrum at MJO scales is realistic (Fig. 3), it arises from a local distribution of intraseasonal variance that is very much different than observed. With regard to air–sea interaction, the lack of variance across the equatorial Indian Ocean would be expected to limit the impact of coupling there.

4. Composite MJO

In an attempt to diagnose why coupling has such little impact on the MJO in this model, composites of the MJO, with emphasis on the structure of the surface fluxes and associated SST anomalies, are formed for the coupled model and for observations. Composites formed for the uncoupled model are nearly identical to those for the coupled model, except, of course, there are no SST anomalies in the uncoupled model. The composites are formed by lag regression of specified fields onto filtered precipitation (model) or OLR (observations) at the base point (0°, 150°E). The use of OLR as a proxy for observed moist convection associated with the MJO is expected to yield smoother but otherwise similar results to other more direct measurements of precipitation (e.g., Microwave Sounding Unit precipitation; Maloney and Hartmann 1998).

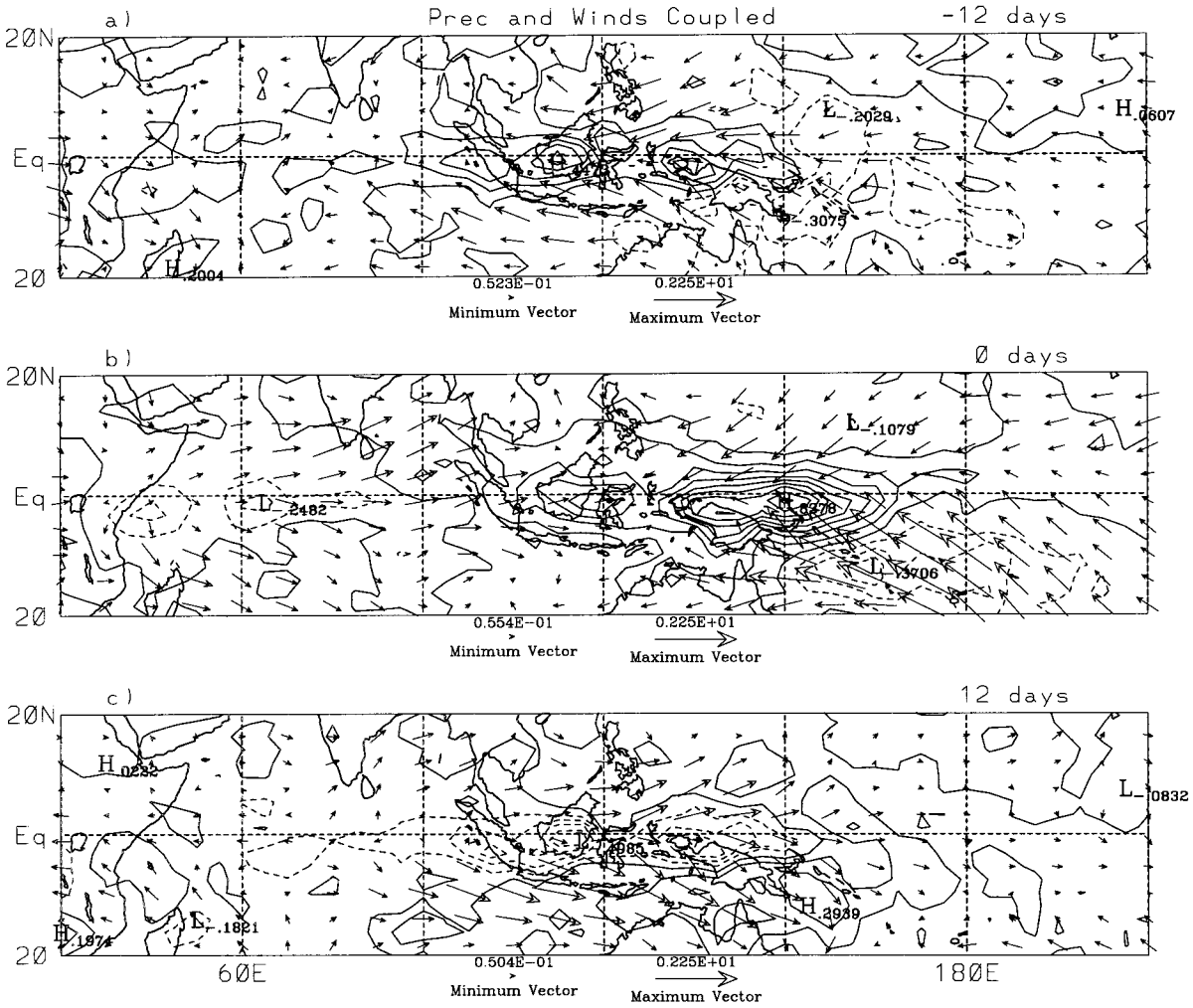

FIG. 7. Regression of precipitation and surface winds from the coupled model onto precipitation at the base point (0°, 150°E) for (a) lag −12 days, (b) lag 0 days, and (c) lag +12 days. Precipitation at the base point was filtered to eastward wavenumbers 1–3 for periods of 35–90 days. Anomalies are shown for a 1.5 standard deviation anomaly of the base point ($=3.3 \times 10^{-1}$ cm day^{-1}). Contour interval for precipitation is 1×10^{-1} cm day^{-1}. The maximum amplitude of the wind vectors is 2.25 m s^{-1}.

Following the technique of Hendon and Salby (1994) precipitation and OLR at the base point are filtered to eastward zonal wavenumbers 1–3 for periods of 35–90 days, in order to emphasize the large-scale eastward propagating components of the MJO. The regression is formed by inverse Fourier transform of the cross power between the base point and the specified field at each grid point. Data for the 180-day segment beginning 15 October each year are used, in order to emphasize the structure of the MJO during the season in which it is observed to be most dominant. The regressed fields are displayed for a 1.5 standard deviation anomaly of the base point.

The composite surface winds and OLR from observations and surface winds and precipitation from the coupled model are shown in Figs. 6 and 7, respectively, for lags of −12, 0, and +12 days. Similar plots for the SST and surface pressure anomalies are shown in Figs. 8 and 9. The sign of OLR at the base point for the observed regression was switched in order to be consistent with the regressions of the model data onto precipitation. The amplitude of the surface wind anomalies is slightly larger for the model composite but the structure of the wind field and precipitation is dramatically different than observed. The observed convective anomalies (Fig. 6) are centered near the equator with Gaussian-like meridional structure extending 15°–20° latitude. They propagate zonally from the Indian Ocean at day −12 to the date line by day +12. Surface westerlies extend about two-thirds of the way across the convective anomaly in the Indian Ocean (day −12) and all the way across the convective anomaly when it has moved to the date line (day +12). Some indication of meridional convergence, associated with frictionally induced downgradient flow in the Kelvin structure that extends eastward along the equator from enhanced convection (Fig.

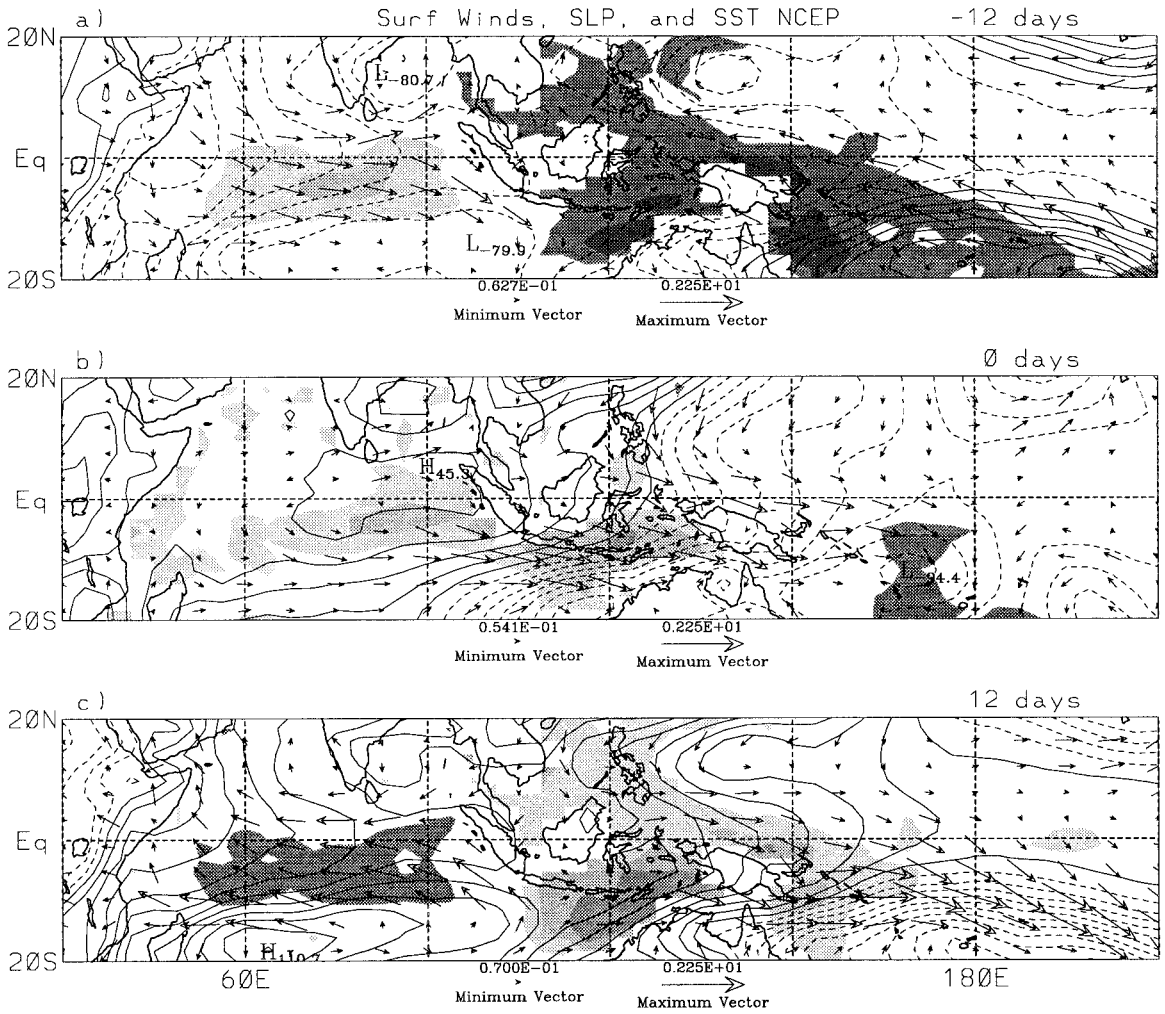

FIG. 8. As in Fig. 6 except for observed SST (shaded), sea level pressure (contoured), and surface winds (vectors) regressed onto OLR at the base point (0°, 150°E). Contour interval for sea level pressure is 10 Pa. Shading levels for SST begin at 0.05°, 0.10°, and 0.15°C, with positive anomalies in dark shades and negative anomalies in light shades. Plotting convention for vector wind is as in Fig. 6.

8), is apparent. However, this convergence is much less pronounced than that diagnosed by Hendon and Salby (1994) using uninitialized analyses from the European Centre for Medium-Range Weather Forecasts.

The model composite (Fig. 7), on the other hand, exhibits precipitation anomalies with much more narrow meridional structure and less coherent zonal propagation. Some narrowing of the meridional extent of precipitation anomalies compared to OLR anomalies is expected [e.g., contrast Hendon and Salby (1994) with Maloney and Hartmann (1998)], but the model's precipitation anomalies actually change sign between the equator and 10°S in the vicinity of 150°E. Consistent with the horizontal distribution of intraseasonal variance (Fig. 5), the model's precipitation anomalies are confined primarily to the north and east of Australia, with some extension into the South Pacific convergence zone (SPCZ). In contrast to the observed behavior, near-equatorial *easterlies* extend all the way across the positive precipitation anomaly at day −12 and about two-thirds of the way across at day 0. By day +12, near equatorial westerlies extend all the way across the negative precipitation anomaly over the Maritime Continent, but surface westerlies do cover the limited region of positive precipitation south of the equator that extends into the SPCZ. The model also exhibits strong downgradient convergent meridional winds to the east of the convection (Fig. 9). This suggests that frictional wave CISK may be playing a important role in the model.

The different phasing of the surface zonal wind relative to the convective anomaly for the model MJO as compared to the observed MJO has important implications for the surface heat flux anomalies (primarily latent heat flux) and for air–sea interaction (discussed below). While the fundamental cause of the MJO is not the topic of this study, it is apparent that the occurrence

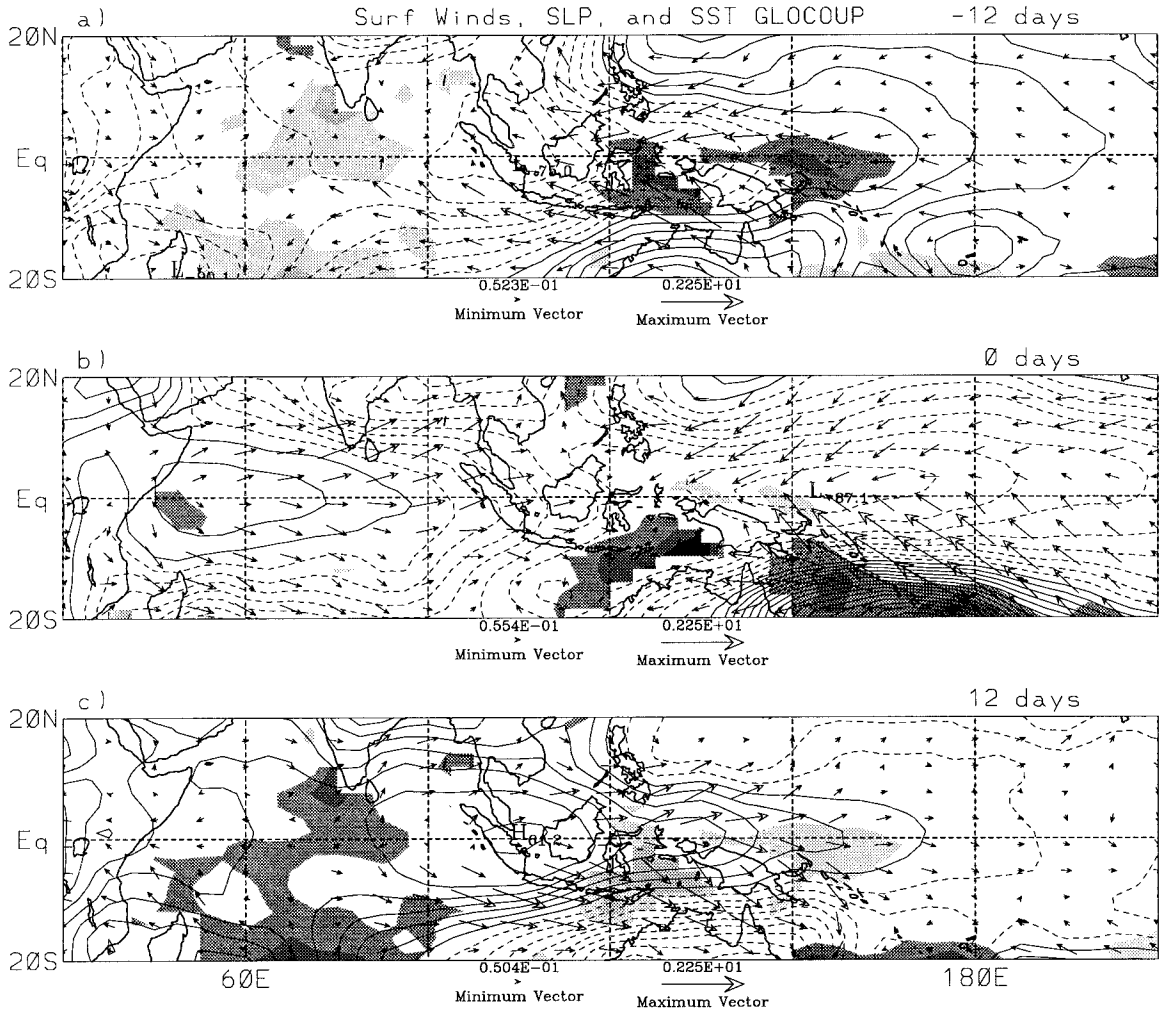

FIG. 9. As in Fig. 7 except for SST (shaded), sea level pressure (contoured), and surface winds (vectors) from the coupled run regressed onto precipitation at the base point (0°, 150°E). Plotting convention is as in Fig. 8.

of easterlies extending through the near-equatorial convective anomaly in the far western Pacific, in conjunction with the easterly bias in the model's mean state (Fig. 1), is such to support evaporation–wind feedback (e.g., Emanuel 1987). This has been shown to play an important role for the MJO in previous versions of the GFDL GCM (e.g., Neelin et al. 1987). Subsequent experimentation with a Gill (1980) steady-state model (B. Mapes 1999, personal communication) suggests that the extension of surface easterlies through the equatorial convective anomaly results from the occurrence of off equatorial heating anomalies near 10°S with opposite sign to those along the equator.

The composite SST anomalies from observations and the coupled model are shaded in Figs. 8 and 9, respectively. Compared to observations, the SST anomalies from the coupled model are weaker, less spatially coherent, and do not extend as far eastward along the equator in the western Pacific. The observed SST anomalies exhibit the required phase relationship with the surface pressure anomalies (contours in Fig. 8) to support positive feedback as discussed by Wang and Xie (1998) and Waliser et al. (1999). That is, across the Maritime Continent and into the western Pacific, equatorial SST anomalies are negatively correlated with surface pressure anomalies. Following Lindzen and Nigam (1987), these SST anomalies are estimated to reduce hydrostatically the surface pressure anomalies by about 10%. Hence, both the zonal and meridional pressure gradients are increased and thus the strength of the surface circulation is increased. The model SST anomalies, besides being significantly weaker than observed, exhibit much less negative correlation with the surface pressure anomalies (they even exhibit pronounced positive correlation across much of the Indian Ocean), hence little feedback is implied.

The cause of the weaker and less spatially coherent than observed SST anomalies and lack of positive feedback in the model is explored by examining how the SST anomalies are formed. Figure 10 displays Hov-

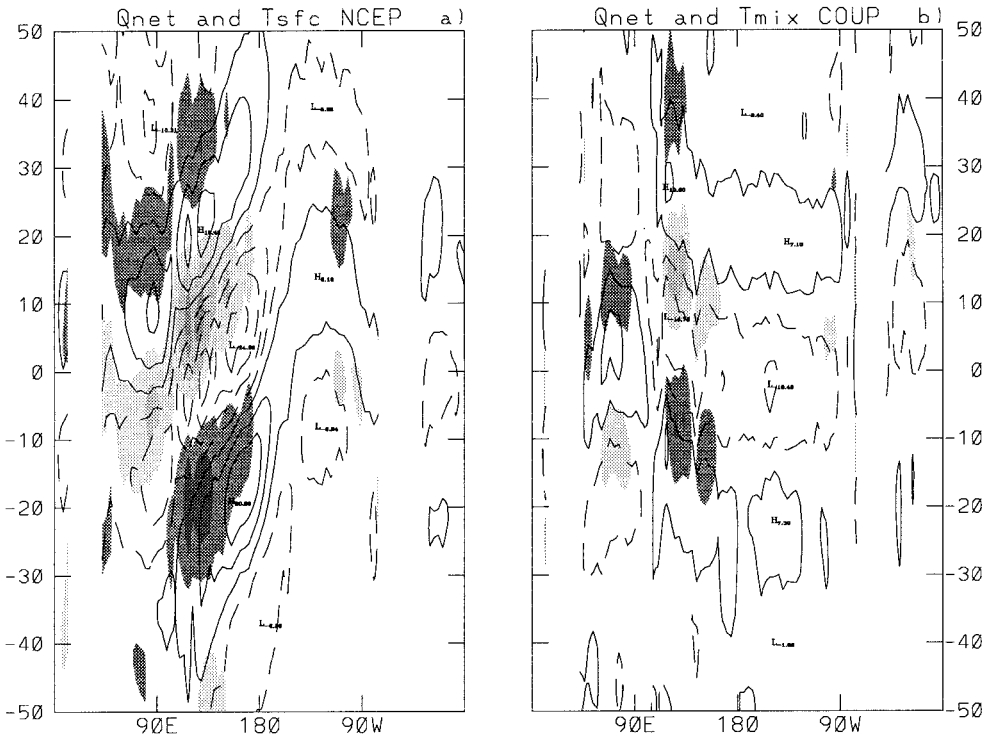

FIG. 10. Hovmöller plot (longitude vs days) of the regression of (a) net surface heat flux and SST from NCEP–NCAR reanalysis onto OLR at the base point (0°, 150°E) and (b) net surface heat flux and SST from the coupled model regressed onto precipitation at the base point (0°, 150°E). The base points were filtered to eastward wavenumbers 1–3 for periods 35–90 days. Regressed anomalies are shown for 1.5 std dev anomalies of the respective base points and were averaged over 5°N–15°S. Contour interval for net surface heat flux is 6 W m^{-2}. Shading levels for SST are as in Fig. 8.

möller representations of the composite net surface heat flux into the ocean and SST anomalies from observations and the coupled model. Anomalies are averaged over 10°S–5°N. The observed heat flux and SST anomalies systematically propagate eastward in unison from the Indian Ocean to about the date line. They exhibit a distinct quadrature realtionship, indicative that the surface heat flux variations are the primary cause of the SST anomalies across the warm pool (see also Shinoda and Hendon 1998). The surface heat flux and SST anomalies from the model, while necessarily exhibiting a quadrature relationship, are much weaker than observed and exhibit little indication of systematic eastward propagation. Hence, the lack of any substantial impact of coupling on the model's MJO stems from the unrealistic evolution and weaker than observed surface heat flux variation, which thus results in weaker than observed SST anomalies that do not have the correct systematic phasing with surface pressure to support feedback.

The cause of the poor simulation of the surface heat flux variation is explored by examination of the two dominant components of the surface heat flux, namely, net shortwave radiation and latent heat flux (Fig. 11). For the observed MJO, these two components act together from the Indian Ocean to about the date line, with enhanced latent heat flux slightly lagging decreased shortwave radiation. The shortwave radiation anomaly from the model exhibits realistic amplitude and eastward propagation across the warm pool, but the model's latent heat flux anomalies are weaker than observed and do not exhibit systematic eastward propagation. The net effect is that the model's shortwave radiation and latent heat flux anomalies range from being out of phase to in quadrature to being in phase across the warm pool, which thus results in limited systematic net heat flux variation.

The weaker amplitude of the latent heat flux anomalies, despite realistic amplitude of the surface wind anomalies, results from larger than observed mean surface specific humidity, cooler than observed mean SST ($\sim$0.25°C), and the relatively weak (1×10^{-3}) exchange coefficient specified in the model's bulk aerodynamic flux parameterizations. The lack of systematic eastward propagation of the model latent heat flux anomalies, despite systematic eastward propagation of the surface zonal wind anomalies (Fig. 12), reflects the lack of mean surface westerlies across the warm pool. While enhanced latent heat flux is observed to result from enhanced surface westerlies across the entire warm pool, enhanced westerlies in the model cause positive latent

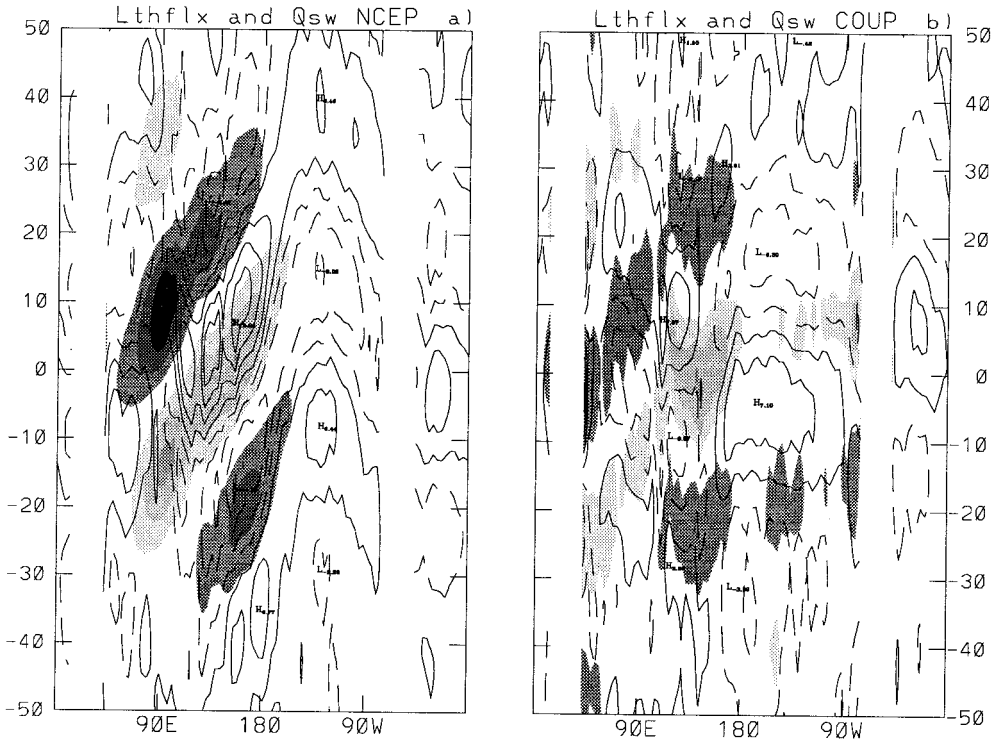

FIG. 11. As in Fig. 10 except for latent heat flux and surface shortwave radiation from (a) NCEP–NCAR reanalysis and (b) the coupled run. Contour interval for latent heat flux is 3 W m^{-2}. Shading levels for shortwave radiation begin at 5, 10, and 15 W m^{-2}, with positive anomalies in dark shades and negative anomalies in light shades.

heat flux anomalies only in a limited domain to the northwest of Australia, where the mean surface wind is westerly. Across the bulk of the equatorial Indian and western Pacific Oceans, enhanced surface westerlies act to reduce the total wind speed and thus result in negative latent heat flux anomalies.

5. Conclusions

The impact of air–sea coupling on the MJO was investigated with a GCM coupled to a comprehensive one-dimensional ocean mixed layer model at each grid point. The rationale for using a comprehensive mixed layer ocean model, rather than a simple slab mixed representation, is that observed intraseasonal variations of the mixed layer associated with the MJO result from the combined effects of the surface fluxes of heat, momentum, and freshwater (Shinoda and Hendon 1999). Accordingly, over the life cycle of the MJO the mixed layer depth varies, which changes the sensitivity of the mixed layer temperature to the heat flux forcing. Furthermore, during the calm–clear phase of the MJO, the mixed layer shoals to ~10 m and penetration of shortwave radiation through the base of the mixed layer becomes significant. Hence, simulation of the mixed layer variations over the life cycle of the MJO requires a model that includes all of these processes (Shinoda and Hendon 1999).

Previous modeling studies, with simple representations of the ocean mixed layer, have found that coupling improved many shortcomings of the simulation of the MJO in uncoupled GCMs, including increasing the amplitude, decreasing the phase speed, and improving the seasonality (e.g., Waliser et al. 1999). Interestingly, the MJO in the uncoupled model used in this study did not suffer from all of these shortcomings. The uncoupled model produces realistic concentration of power at eastward wavenumbers 1–3 and periods 35–90 days. The amplitude of the model's MJO during southern summer, when the observed MJO is most dominant, is also quite realistic. However, intraseasonal variations of surface winds and precipitation associated with the MJO in the uncoupled model are too concentrated to the north and east of Australia with too little extension into the equatorial Indian and far western Pacific Oceans. Also, the MJO in the uncoupled model during northern summer is more than twice as strong as observed. Coupling had little, if any, impact on any of these problems. It furthermore had little impact on any other aspect of the MJO, including changing its phase speed and amplitude.

The mechanism for feedback of the SST anomalies onto the MJO, both observed and diagnosed in other

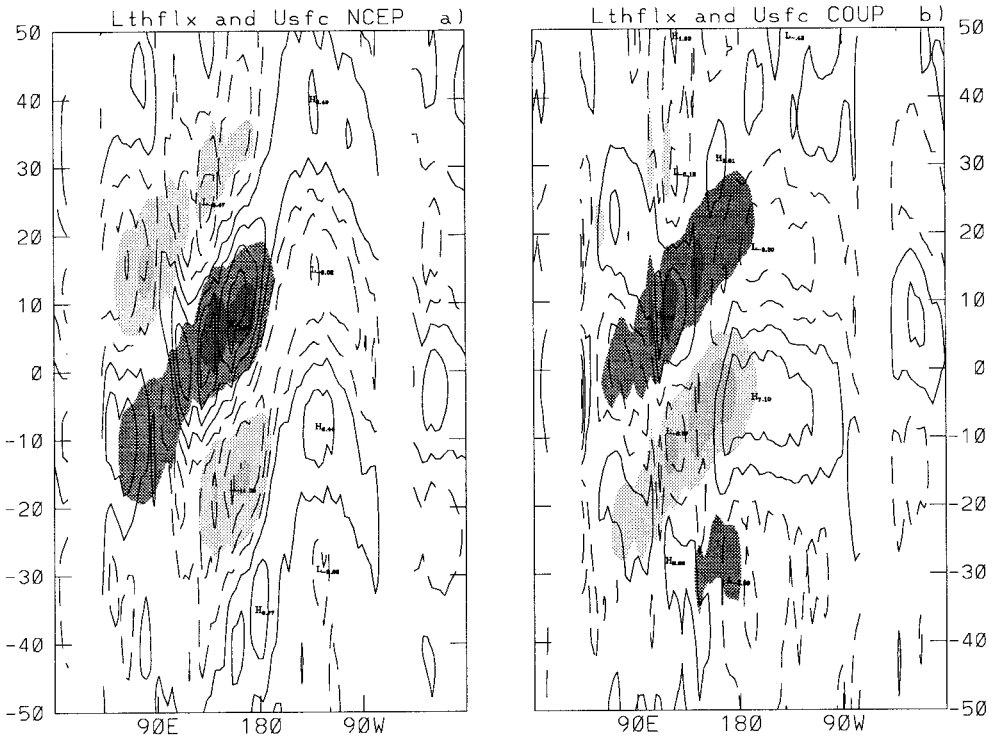

FIG. 12. As in Fig. 10 except for latent heat flux and surface zonal wind from (a) NCEP–NCAR reanalysis and (b) the coupled model. Contour interval for latent heat flux is 3 W m^{-2}. Shading levels for zonal wind begin at 0.5, 1.0, and 1.5 m s^{-1}, with positive anomalies in dark shades and negative anomalies in light shades.

coupled models (e.g., Wang and Xie 1998; Waliser et al. 1999) appears to result from correlation of positive equatorial SST anomalies across the warm pool with surface low pressure in the Kelvin structure to the east of the convective anomaly. The warm SST anomaly acts to reduce the pressure hydrostatically and thus increase the convergent surface circulation. This feedback is not significant in the present coupled model because the SST anomalies do not systematically exhibit the requisite phasing with the surface pressure anomalies and are weaker and less spatially coherent than observed.

The lack of large-scale, spatially coherent SST anomalies with the appropriate phasing with surface pressure necessary for positive feedback stems from problems with the model's surface heat flux. The surface heat flux anomalies produced by the observed MJO result from a combination of shortwave radiation and latent heat flux, whereby enhanced cloudiness associated with enhanced convection slightly leads enhanced latent heat flux associated with enhanced surface westerlies. The observed shortwave and latent heat flux anomalies propagate eastward in unison from the Indian Ocean to near the date line, and they act together to perturb the surface heat flux across the entire warm pool. They act to increase the SST in the tongue of low pressure beneath the easterly Kelvin structure to the east of enhanced convection. While the model's MJO does produce realistic anomalies of shortwave radiation and surface zonal wind that propagate eastward across the warm pool, the associated latent heat flux is not as spatially coherent, does not systematically propagate eastward, and does not systematically add to the shortwave radiation anomaly. Furthermore, the model's latent heat flux anomalies are weaker than observed. Little coherent eastward propagating net surface heat flux anomaly is thus produced. The heat flux anomalies that are produced do not produce SST anomalies that are systematically phased with surface pressure so as to provide positive feedback.

The deficiencies of the model's latent heat flux stem from a variety of problems. First, the lack of mean surface westerlies across much of the warm pool during southern summer, means that enhanced surface westerlies will tend to produce negative, rather than positive, latent heat flux anomalies. Second, the unrealistic phasing of the near equatorial surface zonal wind anomalies relative to the precipitation anomalies in the model, whereby surface easterlies (rather than westerlies) tend to blow most of the way across regions of enhanced equatorial precipitation, results in an unrealistic phasing of the latent heat flux relative to the shortwave anomalies, even in regions of mean westerlies to the north of Australia. Finally, the model's latent heat flux anomalies are weaker than observed because the model's surface humidity is too large, the warm pool SST is too

cool, and a relatively weak exchange coefficient in the bulk flux algorithm was used.

It is interesting to speculate that a similar lack of impact from coupling would have been obtained if the simpler slab mixed layer used by Waliser et al. (1999) were employed here. That is, the problems with the surface heat fluxes produced by the MJO in this version of the GFDL GCM would swamp any inadequacies introduced by the simple slab mixed layer formulation. It would be of interest, however, to couple the GCM used by Waliser et al., which did produce realistic coupled behavior with positive overall benefits for the simulated MJO, to the comprehensive mixed layer model used here. The impact of freshwater and momentum fluxes and penetrative shortwave radiation, thought to be important for the evolution of the mixed layer over the life cycle of the MJO (Shinoda and Hendon 1998), on the coupled behavior could then be examined.

The null result for the present coupled model thus emphasizes two points. The first is that coupling is not a panacea for the problems of simulating the MJO in an uncoupled GCM. However, if coupled behavior across the warm pool is important for the dynamics of the MJO, then the model needs to simulate an MJO with a proper distribution of surface fluxes.

Acknowledgments. Mike Alexander and Jamie Scott implemented the uncoupled and coupled models at CDC. They kindly made available to me their coupled and control runs. J. Scott also provided invaluable help with accessing the model data. Constructive comments by three anonymous reviewers are gratefully acknowledged. This research was supported by TOGA COARE and GOALS grants from NOAA's Office of Global Programs.

REFERENCES

Alexander, M. A., and J. D. Scott, cited 2000: Web-based atlas of climatology and variability in the GFDL R30S14 GCM. [Available online at http://www.cdc.noaa.gov/gfdl.]

——, ——, and C. Deser, 2000: Climate variability in a coupled atmosphere–ocean model: The role of ocean mixed layer processes. *J. Geophys. Res.,* **105,** 16 823–16 842.

Anderson, S. P., R. A. Weller, and R. Lukas, 1996: Surface buoyancy forcing and the mixed layer in the western Pacific warm pool: Observation and one-dimensional model results. *J. Climate,* **9,** 3056–3085.

Emanuel, K. A., 1987: An air–sea interaction model of intraseasonal oscillations in the tropics. *J. Atmos. Sci.,* **44,** 2324–2340.

Feng, M. P., P. Hacker, and R. Lukas, 1998: Upper ocean heat and salt balances in response to a westerly wind burst in the western equatorial Pacific. *J. Geophys. Res.,* **103,** 10 289–10 311.

Flatau, M., P. J. Latau, P. Phoebus, and P. P. Niiler, 1997: The feedback between equatorial convection and local radiative and evaporative processes: The implication for intraseasonal oscillations. *J. Atmos. Sci.,* **54,** 2373–2386.

Gaspar, P., 1988: Modeling the seasonal cycle of the upper ocean. *J. Phys. Oceanogr.,* **18,** 161–180.

Gill, A. E., 1980: Some simple solutions for heat-induced tropical circulation. *Quart. J. Roy. Meteor. Soc.,* **106,** 447–462.

Gordon, C. T., and W. F. Stern, 1982: A description of the GFDL global spectral model. *Mon. Wea. Rev.,* **110,** 625–644.

Gutzler, D. S., G. N. Kiladis, G. A. Meehl, K. M. Weickmann, and M. Wheeler, 1994: The global climate of December 1992–February 1993. Part II: Large-scale variability across the tropical western Pacific during TOGA COARE. *J. Climate,* **7,** 1606–1622.

Hayashi, Y., and D. G. Golder, 1993: Tropical 40–50- and 20–30-day oscillations appearing in realistic and idealized climate models and the ECMWF dataset. *J. Atmos. Sci.,* **50,** 464–494.

Hendon, H. H., and M. L. Salby, 1994: The life cycle of the Madden–Julian oscillation. *J. Atmos. Sci.,* **51,** 2225–2237.

——, and J. D. Glick, 1997: Intraseasonal air–sea interaction in the tropical Indian and Pacific Oceans. *J. Climate,* **10,** 647–661.

——, B. Liebmann, J. D. Glick., M. Newman, and J. Schemm, 2000: Medium range forecast errors associated with active episodes of the Madden–Julian oscillation. *Mon. Wea. Rev.,* **128,** 69–86.

Kalnay, E., and Coauthors, 1996: The NCEP/NCAR 40-year reanalysis project. *Bull. Amer. Meteor. Soc.,* **77,** 437–471.

Krishnamurti, T. N., D. K. Osterhof, and A. V. Mehta, 1988: Air–sea interaction on the time scale of 30–50 days. *J. Atmos. Sci.,* **45,** 1304–1322.

Lau, K.-M., and C.-H. Sui, 1997: Mechanisms of short-term sea surface temperature regulation: Observations from TOGA COARE. *J. Climate,* **10,** 465–472.

Liebmann, B., and C. A. Smith, 1996: Description of a complete (interpolated) outgoing longwave radiation dataset. *Bull. Amer. Meteor. Soc.,* **77,** 1275–1277.

Lindzen, R. S., and S. Nigam, 1987: On the role of sea surface temperature gradients in forcing low-level winds and convergence in the Tropics. *J. Atmos. Sci.,* **44,** 2418–2436.

Maloney, E. D., and D. Hartmann, 1998: Frictional moisture convergence in a composite life cycle of the Madden–Julian oscillation. *J. Climate,* **11,** 2387–2403.

Neelin, J. D., I. M. Held, and K. H. Cook, 1987: Evaporation-wind feedback and low-frequency variability in the tropical atmosphere. *J. Atmos. Sci.,* **44,** 2341–2348.

Salby, M. L., and H. H. Hendon, 1994: Intraseasonal behavior of clouds, temperature, and winds in the Tropics. *J. Atmos. Sci.,* **51,** 2207–2224.

Shinoda, T., and H. H. Hendon, 1998: Mixed layer modeling of intraseasonal variability in the tropical western Pacific and Indian Oceans. *J. Climate,* **11,** 2668–2685.

——, ——, and J. Glick, 1998: Intraseasonal variability of surface fluxes and sea surface temperature in the tropical western Pacific and Indian Oceans. *J. Climate,* **11,** 1685–1702.

——, ——, and ——, 1999: Intraseasonal surface fluxes in the tropical western Pacific and Indian Oceans from NCEP reanalyses. *Mon Wea. Rev.,* **127,** 678–693.

Slingo, J. M., and Coauthors, 1996: Intraseasonal oscillations in 15 atmospheric general circulation models: Results from an AMIP diagnostic subproject. *Climate Dyn.,* **12,** 325–357.

Sperber, K. R., J. M. Slingo, P. M. Inness, and W. K-M. Lau, 1997: On the maintenance and initiation of the intraseasonal oscillation in the NCEP/NCAR reanalysis and in the GLA and UKMO AMIP simulations. *Climate Dyn.,* **13,** 769–795.

Waliser, D. E., K. M. Lau, and J. H. Lim, 1999: The influence of coupled sea surface temperatures on the Madden–Julian oscillation: A model perturbation experiment. *J. Atmos. Sci.,* **56,** 333–358.

Wang, B., and X. Xie, 1998: Coupled modes of the warm pool climate system. Part I: The role of air–sea interaction in maintaining Madden–Julian oscillations. *J. Climate,* **8,** 2116–2135.

Weller, R. A., and S. P. Anderson, 1996: Surface meteorology and air–sea fluxes in the western equatorial Pacific warm pool during the TOGA Coupled Ocean–Atmosphere Response Experiment. *J. Climate,* **9,** 1959–1990.

Zhang, C., 1996: Atmospheric intraseasonal variability at the surface in the western Pacific Ocean. *J. Atmos. Sci.,* **53,** 739–758.